



**HAL**  
open science

## Assessing Coulombic Efficiency in Lithium Metal Anodes

Abdolkhaled Mohammadi, Sabrine Djafer, Syreina Sayegh, Andrew Naylor, Mikhael Bechelany, Reza Younesi, Laure Monconduit, Lorenzo Stievano

### ► To cite this version:

Abdolkhaled Mohammadi, Sabrine Djafer, Syreina Sayegh, Andrew Naylor, Mikhael Bechelany, et al.. Assessing Coulombic Efficiency in Lithium Metal Anodes. *Chemistry of Materials*, 2023, 35 (6), pp.2381-2393. 10.1021/acs.chemmater.2c03518 . hal-04052342

**HAL Id: hal-04052342**

**<https://cnrs.hal.science/hal-04052342>**

Submitted on 14 Oct 2023

**HAL** is a multi-disciplinary open access archive for the deposit and dissemination of scientific research documents, whether they are published or not. The documents may come from teaching and research institutions in France or abroad, or from public or private research centers.

L'archive ouverte pluridisciplinaire **HAL**, est destinée au dépôt et à la diffusion de documents scientifiques de niveau recherche, publiés ou non, émanant des établissements d'enseignement et de recherche français ou étrangers, des laboratoires publics ou privés.

# Assessing Coulombic Efficiency in Lithium Metal Anodes

Abdolkhaled Mohammadi<sup>1,2,3</sup>, Sabrine Djafer<sup>1</sup>, Syreina Sayegh<sup>4</sup>, Andrew J. Naylor<sup>2</sup>, Mikhael Bechelany<sup>4</sup>, Reza Younesi<sup>2,3</sup>, Laure Monconduit<sup>1,3,5</sup>, Lorenzo Stievano<sup>1,3,5\*</sup>

1 ICGM, Univ. Montpellier, CNRS, ENSCM, Montpellier, France

2 Department of Chemistry – Ångström Laboratory, Uppsala University, Uppsala, Sweden

3 Alistore-ERI, CNRS, Amiens, France

4 Institut Européen des Membranes, IEM, UMR 5635, Univ. Montpellier, CNRS, ENSCM, Montpellier, France

5 RS2E, CNRS, Amiens, France

\* Lorenzo.stievano@umontpellier.fr

---

**ABSTRACT:** Although lithium metal and anode-free rechargeable batteries (LMBs and AFBs) are phenomenal energy storage systems, the formation of lithium deposits with high surfaces during repeated plating-stripping cycles has hindered their practical applications. Recently, extensive efforts have been made to prevent the growth of high-surface lithium deposition, e.g., electrolyte modification, artificial coating deposition, lithiophilic current collectors, composite lithium metal electrodes, etc. In most of these approaches, coulombic efficiency (CE) has been used as a quantifiable indicator for the reversibility of the LMBs and AFBs. The interpretation and validation of research results, however, are challenging since the measurement of CE is affected by several parameters related to battery assembly and testing. This study aims to unveil the interplay of several potentially overlooked parameters regulating the CE, such as stripping cutoff voltage, electrolyte quantity, pre-cycling to form solid electrode interphase (SEI), and electrode surface modification, by applying two alternative electrochemical methods. The hidden aspects of nucleation overpotential revealed by studying these parameters, as well as their influence on the composition and stability of the SEI are discussed. Overall, this work provides an insightful understanding of the methods and parameters used for assessing the performance of LMBs and AFBs.

---

## INTRODUCTION

The future generation of rechargeable batteries has to be highly energy-efficient to meet the ever-increasing demands of the electronics industry and electric vehicles<sup>1</sup>. So far, one of the most promising lines of development has been employing lithium metal as the negative electrode in such batteries<sup>2</sup>. Lithium metal is considered the ultimate choice of anode materials because of its high theoretical specific capacity (3860 mAh g<sup>-1</sup>) and lowest electrochemical potential (-3.04 V vs. ESH)<sup>3</sup>. Despite these prominent merits, the industrial deployment of lithium metal batteries (LMBs) has been impeded by the critical problems of low coulombic efficiency (CE) and poor cyclability<sup>4</sup>. The fundamental problem stems from the formation of lithium metal deposits with high surface area (*i.e.*, dendrites, whiskers, mossy lithium) during plating, which in addition to the creation of large reactive surfaces, eventually leads to the formation of inactive lithium (dead lithium) during the stripping process<sup>5-7</sup>. Consequently, lithium metal anodes suffer from poor cycling stability and low CE. More recently, anode-free lithium metal batteries (AFBs), obtained by removing the metallic lithium anode at the initial state, have shown a potential to further increase battery energy density<sup>8-11</sup>. The low CE and poor cycling reversibility reported in the literature for these systems, however, are not satisfactory compared to those of LMBs, mainly because there is no

lithium reservoir to replenish lost lithium. Similar to LMBs, AFBs also suffer from problems originating from the creation of high surface area lithium and the formation of inactive lithium, which is directly correlated with low CE<sup>12-15</sup>. Over the past few decades, extensive efforts have been devoted to understanding the mechanism of the formation of high surface area lithium deposition<sup>16-19</sup> and developing strategies to achieve high CE in LMBs and AFBs, such as developing new electrolyte/additives<sup>20-24</sup>, electrochemical treatments<sup>25-27</sup>, surface engineering<sup>28-31</sup>, solid-state electrolytes<sup>32-34</sup>, and lithium host modification<sup>35,36</sup> and so on<sup>4,37</sup>.

Most previous works highlighted the achievement of high CE, frequently linked to high cycling reversibility with the low surface area electrodeposition of lithium (non-dendrite); however, CE can be easily misunderstood or overlooked especially in half-cells<sup>38</sup>. The measurement of lithium CE is often affected by various factors<sup>39,40</sup>, and the electrochemical measurement methods reported in the literature often give different values, even for the same cell design. Few researchers have explicitly addressed the known parameters in determining the CE of LMBs and AFBs, as well as the tradeoffs between CE and cycling reversibility<sup>38-42</sup>. For example, Xiao et al.<sup>39</sup> discussed the fundamental definition of CE in various cell configurations (*i.e.*, Lithium-ion batteries, LMBs, and AFBs). They examined the comparisons between CE and capacity retention with different types

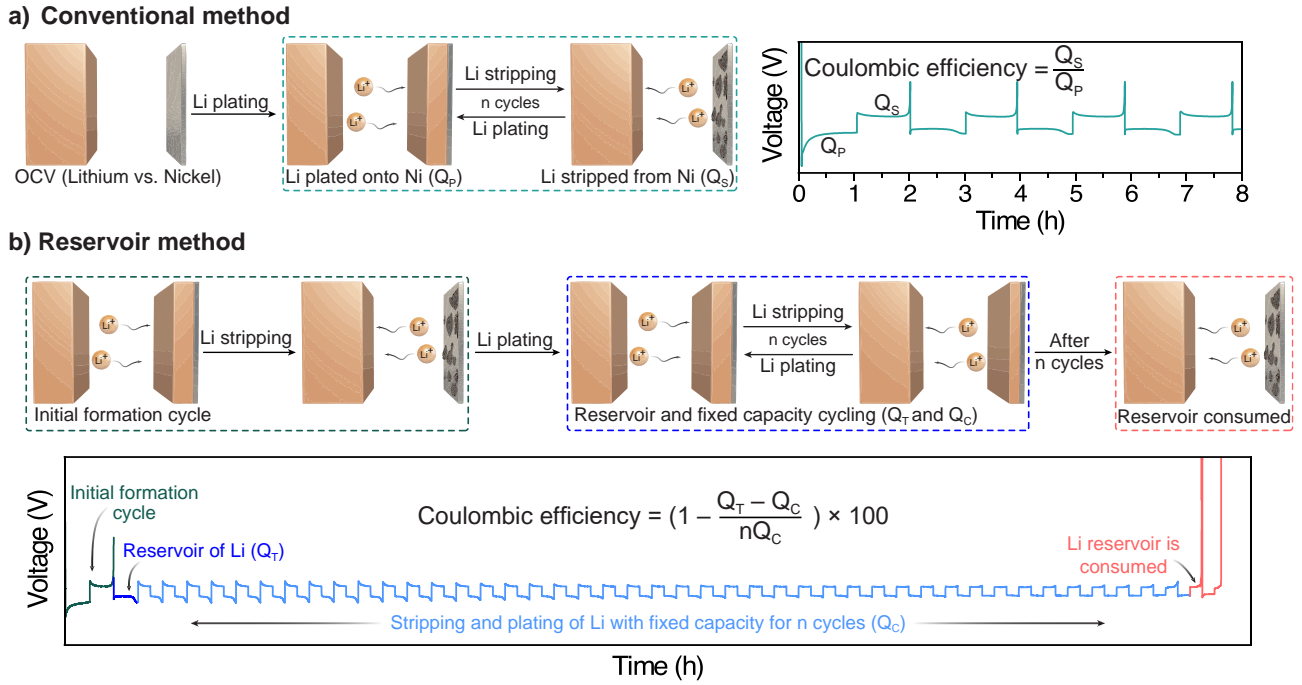


Fig. 1: Evaluation of LMBs and AFBs using half-cell electrochemical methods: schematic description of the methods a) conventional and b) reservoir method.

and quantities of electrolytes. More recently, Winter et al.<sup>41</sup> focused on the reversibility of lithium cycling, regarding a range of experimental parameters, such as current density, capacity, and electrolyte type, in both symmetric (Li || Li) and asymmetric (Cu || Li) configurations. Different methods have also been developed to evaluate the CE of LMBs. Adams et al.<sup>42</sup> developed a new method originating from the Aurbach et al.<sup>43</sup> approaches to more accurately measure the CE based on the reservation of the lithium metal on the electrode surface, also known as the “reservoir method”. Undoubtedly, these types of studies are of great aid in explaining the reported differences and improving the research community’s ability to perform more systematic and viable studies. Still, some key parameters which could have a significant impact on the outcome have been underestimated or not completely considered in the CE measurements.

In this work, two alternative electrochemical methods, defined as “conventional” and “reservoir” (*vide infra*) have been used to investigate the evolution of the CE in ZnO-coated Ni foam current collectors for AFBs. The effect of the modification of the current collector and electrolyte solution on the electrochemical plating and stripping of metallic lithium has already been studied in half-cell setups<sup>10,44–48</sup>. Using three-dimensional (3D) structures coated with lithophilic materials is an approach that has recently received considerable attention<sup>49,50</sup>. As studied previously<sup>51–53</sup>, a thin layer of ZnO on a 3D current collector influences the morphology of deposited lithium and improves electrochemical performance. Here, 3D Ni foam coated by ZnO was used to characterize the CE of LMBs and AFBs. In such a system, the effect of various parameters, often neglected in the study of the CE in LMBs and AFBs, such as upper discharge cutoff voltage, thicknesses of the protective artificial coating, solid electrolyte interphase (SEI) formation, and electrolyte volume will be thoroughly examined. Indeed, the

choice of a reliable electrochemical protocol is critical to correctly correlate the effect of the different parameters. The methods used until now to measure CE and cycling performance of LMBs and AFBs are not always rigorously defined, and they are not always compatible among them, often leading to inconsistent results. It is worth mentioning that the influence of some known parameters, such as current density and electrolyte composition, is not covered here, and the readers are referred to the previous references for more information about them<sup>38–42</sup>.

## RESULTS AND DISCUSSIONS

The two approaches employed to investigate the CE behavior of lithium deposition-dissolution with the half-cell configuration are illustrated in Fig. 1. The so-called “conventional” method (Fig. 1a) is the simplest method and has been often used in the literature to determine CE and cycling stability. It consists of plating a given amount of lithium on the lithium-less working electrode ( $Q_p$ ), followed by stripping until a cutoff voltage ( $Q_s$ ) is reached. This cutoff indicates that all the removable lithium has been stripped from the electrode surface. In this method, the CE can be tracked with the cycle number, and it can be calculated as the ratio between the amount of lithium stripped from the substrate and the previously plated lithium, as indicated in Eq. 1.

$$CE = \frac{\text{Stripping capacity } (Q_s)}{\text{Plating capacity } (Q_p)} \times 100\% \quad \text{Eq. 1}$$

Recently, Adams et al.<sup>42</sup> modified the Aurbach et al.<sup>43</sup> approach, known as the “reservoir” method, and proposed a new method to determine the average CE, as shown in Fig. 1b. A single lithium deposition–dissolution cycle is used in this method to produce the SEI on the electrode surface. Next, the lithium reservoir ( $Q_T$ ) is plated on the electrode,

and then the battery undergoes continuous stripping/plating cycles with a fixed capacity lower than the initial lithium reservoir ( $Q_C < Q_T$ ) for  $n$  cycles. The side reactions gradually consume the lithium reservoir during cycling<sup>42,51</sup>, and eventually, after  $n$  cycles, the lithium reservoir is completely depleted, as indicated by the sharp increase of the stripping potential. In this method, the average CE over  $n$  cycles can be calculated by using Eq. 2, which is a first-order expansion of Eq. 1:

$$CE = \left(1 - \frac{Q_T - Q_C}{nQ_C}\right) \times 100\% \quad \text{Eq. 2}$$

In the following section, we will discuss how and why several parameters, such as stripping cutoff voltage, pre-cycling SEI formation, modification of electrode surface, and electrolyte amount, substantially impact the CE measurements in conventional and reservoir methods. Noted that the electrolyte chosen to carry out this work (1M LiTFSI in DOL / DME (1/1 vol.) with 2 wt.% of LiNO<sub>3</sub>) had already been widely used in the literature for LMBs and AFBs since recognized for its high cycling stability and optimal coulombic efficiency<sup>54,55</sup>.

### Influence of the cutoff voltage

Researchers have shown that the upper cutoff potential is critical for transition metal oxide cathode materials since capacity fade is accelerated in the higher upper cutoff potential<sup>56,57</sup>. Likewise, the upper cutoff voltage is an influential parameter that impacts the electrochemical performance of LMBs and AFBs<sup>58,59</sup>. The effect of upper cutoff voltage on the plating-stripping cycling performance was evaluated by using different cutoff potentials of 0.5 V, 1.0 V, 1.5 V, and 0.2 V (Fig. 2a and S1). Setting the stripping voltage to the lower cutoff voltages results in the limitation of conversion-dealloying and re-alloying processes, plating and stripping thus becoming the main processes<sup>60-62</sup>. Fig. 2b shows that, after stabilization in the first 20 plating/stripping cycles, the CE value slightly increases with increasing cutoff voltage. Nevertheless, as shown in the table inset of Fig. 2b, the fluctuation of the CE, measured as the standard deviation of CE values between cycles 20 and 160, increases from 0.5 % to 0.8 % for 0.2 V to 1.5 V cutoff voltages, respectively. A control sample without ZnO was used to evaluate the CE fluctuations observed at higher voltages. Despite the absence of ZnO, the fluctuation was still visible (Fig. S2 in the Supporting Information). This suggests that factors such as SEI evolution or reactivation of trapped lithium could be contributing to the CE fluctuations, rather than the conversion-dealloying and re-alloying processes reaction of ZnO. More importantly, longer cycle life is observed for lower cutoff voltages, which is attributed to lower electrolyte decomposition and irreversible electrochemical reactions, as discussed later. Therefore, it is recommended to lower the cutoff voltage to increase the cycle life. Hence, a 0.2 V cutoff voltage was chosen for the following electrochemical analyses.

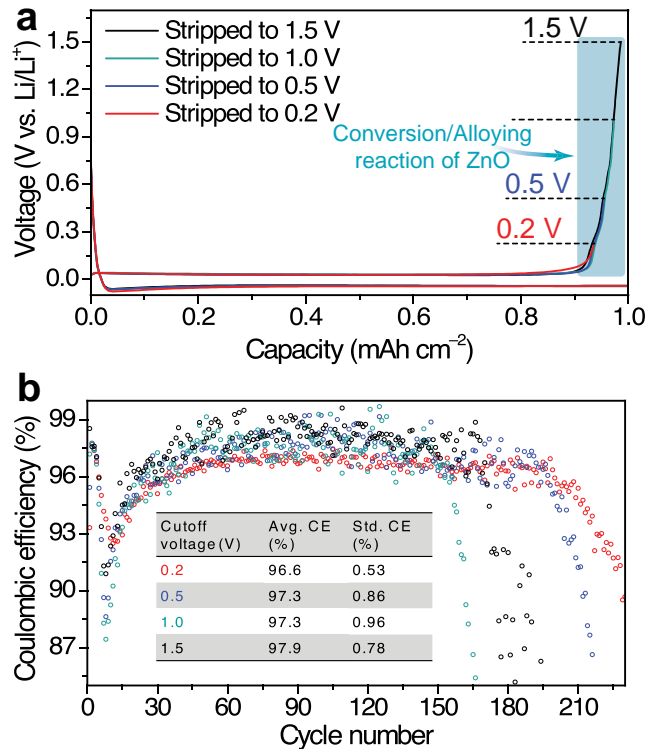
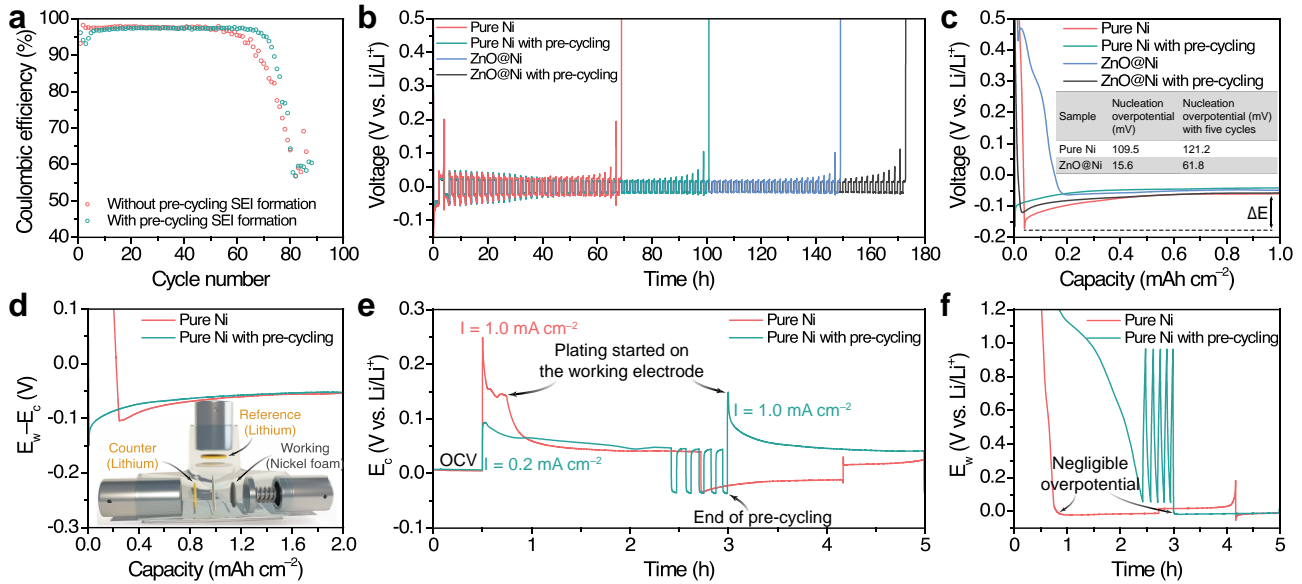


Fig. 2: **Influence of stripping cutoff on the CE and cycling stability of conventional electrochemical method:** a) voltage versus capacity profile of ZnO with 25 nm thickness coated Ni foam and b) cyclic performance and CE dependence for the different cutoff voltages of 0.2, 0.5, 1.0, and 1.5 V at the current density of 1 mA cm<sup>-2</sup> and capacity of 1 mAh cm<sup>-2</sup>.

### Influence of pre-cycling

In several previously published papers, several discharge/charge cycles in a potential range above 0 V vs. Li<sup>+</sup>/Li are applied to the cell to stabilize the SEI before starting the plating/stripping process<sup>63</sup>. However, to the best of our knowledge, a comprehensive study on the influence of this pre-cycling procedure on CE and the cycling stability of the following plating/stripping process has not been conducted. To verify its effects, several cells pre-cycled five times between 0.01 V and 1 V at 0.2 mA cm<sup>-2</sup> were compared to cells where pre-cycling was not applied. During the discharge, lithium reduces the thin layer of native oxides on the surface of the Ni foam substrate by an irreversible conversion reaction (e.g., NiO + 2Li<sup>+</sup> + e<sup>-</sup> → Ni<sup>0</sup> + Li<sub>2</sub>O)<sup>64</sup>. When ZnO-coated Ni foam is used, lithium ions react with ZnO and form Li<sub>2</sub>O and LiZn via a conversion reaction followed by alloying<sup>65</sup>. The ZnO-coated sample provides a higher capacity than non-coated Ni foam between 0.01 and 1 V (*cf.* Fig. S3). As shown in Fig. 3a, almost no differences in the cycling stability are observed for the cells with and without pre-cycling when using the conventional method of plating-stripping. The stabilized SEI can probably be easily changed and damaged by the following lithium stripping and plating cycles. However, pre-cycling has a clear beneficial influence on the cycling performance when using the reservoir method (Fig. 3b). This can be explained by the fact that the initial SEI layer formed during the pre-cycling remains intact as the initially plated lithium reservoir is not com-



**Fig. 3: Comparison of the effect of SEI activation on electrochemical performance and relationship between cell performance and nucleation overpotential:** a) cycling performance and CE measurement with the conventional method w/o SEI activation of pure Ni sample with 50  $\mu\text{l}$  of electrolyte, b) voltage curves of reservoir method for the Ni and ZnO-coated Ni electrodes w/o SEI activation, c) impact of SEI activation cycle on the nucleation overpotential of the first half-discharge of the samples (inset table represented the measured nucleation overpotential). Measurement of nucleation overpotential in three-electrode Swagelok T-cell w/o SEI activation: d) overall voltage profile, e) counter electrode, and f) working electrode contribution.

pletely stripped. These results are consistent with the discussion in the later section (*vide infra*) where it will be shown how SEI will change during cycling, thereby altering the mechanism of cell failure.

The results show that by applying five cycles of SEI stabilization, the nucleation overpotential increases from 109.5 to 121.2 mV for non-coated Ni foam and from 15.6 to 61.8 mV for ZnO-coated Ni (Fig. 3c). Several studies have demonstrated that the nucleation overpotential, defined as the voltage difference between the lowest point and higher flat segment of voltage ( $\Delta E$ , Fig. 3c) is a key parameter providing information related to lithium deposition and lithiophilicity of the electrodes which influence the battery performance<sup>66–69</sup>. In particular, a lower value of nucleation overpotential should indicate more favorable and smoother lithium electrodeposition via more homogeneous nucleation and a reduced formation of lithium dendrites, with a subsequent improvement of the electrochemical performance. This is not the case in the results shown in Fig. 3, where the cells with higher initial nucleation overpotential show the best cycling stability when using the reservoir method. In order to investigate the existence of a possible relationship between nucleation overpotential and cell performance, specific analyses were carried out using a Swagelok three-electrode T-cell. Fig. 3d shows the overall voltage profile of the Swagelok T-cell electrode ( $E_{\text{working}} - E_{\text{counter}}$ ). Similar to the results obtained in two-electrode coin cells, the nucleation overpotential is higher for the cell submitted to the pre-cycling procedure. The voltage of the counter electrode (Fig. 3e) sharply increases, while the working electrode (Fig. 3f) shows almost no drop in the potential during lithium plating for both cells. Once the plating starts, the counter electrode potential experiences a gradual decrease until

a stable state is reached, which appears in the overall potential during the lithium deposition process. The surface area associated with the creation of pits on the surface of lithium metal continues to increase on the counter electrode during the process, resulting in decreasing potential of the counter electrode and overall cell polarization<sup>70,71</sup>. It means that the energy necessary to activate lithium stripping at the lithium metal counter electrode is much higher than that necessary for forming nucleation sites on the working electrode. In conclusion, there is no correlation between the nucleation overpotential and the performance of the batteries since the so-called nucleation overpotential simply does not correspond to the effective activation energy for the formation of lithium metal plating nuclei.

Furthermore, another question was raised about the observation of a lower nucleation overpotential in lithiophilic materials. In this case, to pinpoint the source of the nucleation overpotential in lithiophilic materials, ZnO-coated Ni foam (as a lithiophilic electrode) was used as the working electrode and compared with uncoated Ni (Fig. S4). As shown in Fig. S4b, it is evident that during lithium plating, for both uncoated and ZnO-coated Ni electrodes there is a constant voltage decrease to a steady-state level in the working potential. As shown in Fig. S4c, the initial drop in cell potential is predominantly due to the sudden drop in the counter electrode potential, which, as explained, could be due to the pitting effect on the lithium metal surface of the counter-electrode. In the ZnO-coated sample, the plating peak in the counter electrode shifts to a lower overpotential because of the extra capacity required for the conversion-alloying reaction. This extra capacity is responsible for reducing the observed nucleation overpotential in the ZnO-coated electrode compared to the uncoated Ni electrode. Note that the

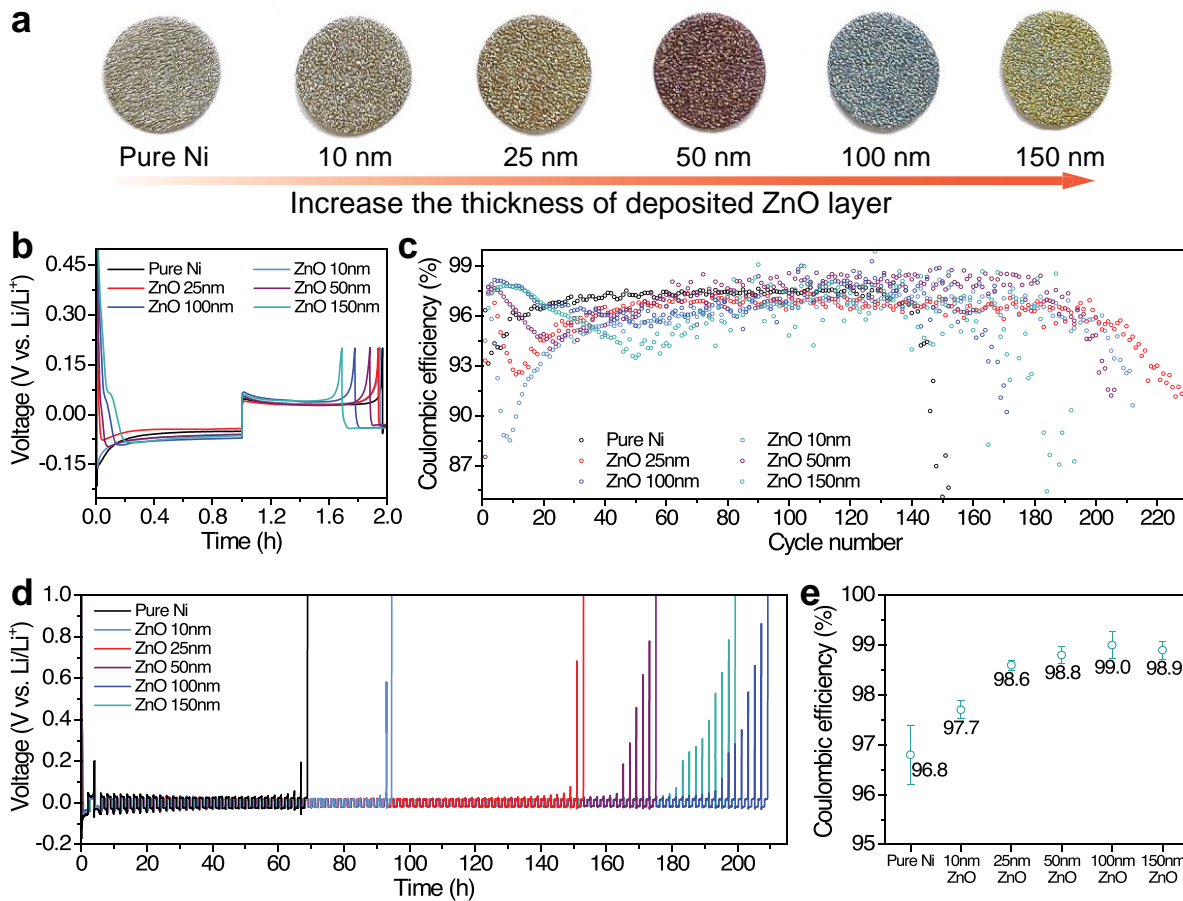


**Fig. 4: Modification of electrode surface:** a) Photographs of Ni foam after being coated with various thicknesses of ZnO layer, b) Impact of ZnO layer thickness on the first cycle CE, c) cyclic and CE performance comparison with a conventional method with the current density of  $1.0 \text{ mA cm}^{-2}$  and capacity of  $1.0 \text{ mAh cm}^{-2}$ , d) cycle life performance in reservoir method at the current density of  $1.0 \text{ mA cm}^{-2}$ , reservoir capacity of  $2.0 \text{ mAh cm}^{-2}$ , and fixed cycling capacity of  $1.0 \text{ mAh cm}^{-2}$  and e) average CE calculated using reservoir method with different thicknesses of ZnO coated Ni foam (The error bars were calculated by taking the standard errors from the measurements with three identical samples).

nucleation overpotential is dominated by the working electrode in the second half-discharge cycle, unlike the first half-cycle, which should account for a true nucleation overpotential of the system, in line with our previous report<sup>70</sup> and the report by Seok et al.<sup>71</sup>. These results collectively indicate that the origin of the nucleation overpotential is largely overlooked as an indicator of the energy required to form the lithium nucleation, leading to misguided data interpretation.

### Modification of electrode surface

A recent trend among papers has been to modify current collectors to improve lithium nucleation and growth behavior<sup>49,50,72-74</sup>. Previously we have shown that the use of ZnO-coated Ni foam leads to the formation of lower surface area lithium and overall leads to better electrochemical performance<sup>75</sup>. Yet, achieving maximum electrochemical performance requires the optimization of ZnO layer thickness. For this reason, five Ni foam substrates coated with ZnO layers of increasing thickness going from 10 to 150 nm were prepared by atomic layer deposition (ALD). Based on the scanning electron microscope (SEM) and X-ray photoelectron

spectroscopy (XPS) analysis, it was concluded that ZnO homogeneously covered the surface of the Ni foam. A detailed discussion of the SEM and XPS measurement can be found in the Supplementary information in Fig. S5. As previously done in the literature<sup>10,44,51,76-79</sup>, both the reservoir and the conventional methods were used to evaluate their performance and determine the optimal thickness of the coating layer. As shown in Fig. 4a, the prepared samples show different colors due to interference effects in the thin ZnO layers of varying thicknesses. Before measuring the CE, a pre-cycling procedure consisting of five cycles was used to form the SEI, as shown in Fig. S6. Since the samples coated with thicker ZnO layers logically contain more zinc oxide, their pre-cycling procedure, which corresponds to the conversion alloying of zinc results in longer reaction times. A comparison of the first cycle CE with the thickness of the ZnO layer is shown in Fig. 4b. The thickness of the ZnO layer significantly impacts the CE for the first cycle, and by increasing the thickness, lithium consumption increases. There has been a change in the nucleation and lithium growth overpotentials upon plating for different thicknesses of ZnO. According to the three-electrode system previously discussed, the counter electrode is most likely the main contributor.

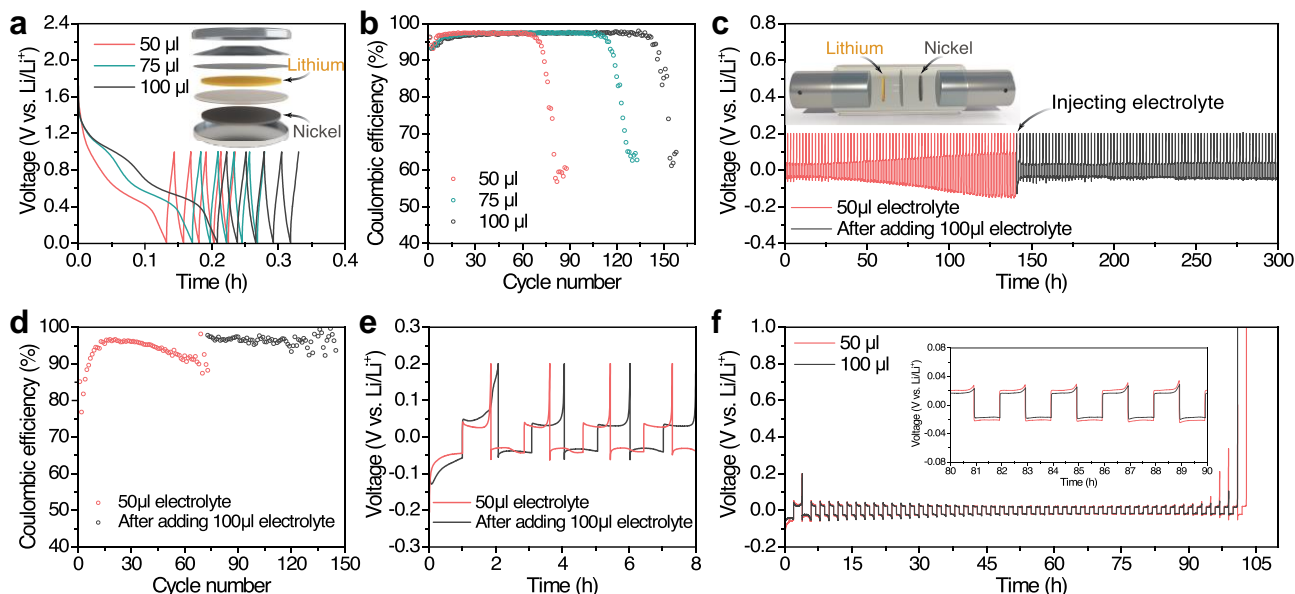


**Fig. 5: Study of the effect of quantity of electrolyte:** (a - e) conventional method, a) comparison of SEI formation cycle at  $0.2 \text{ mA cm}^{-2}$  in coin cells containing  $50 \mu\text{L}$ ,  $75 \mu\text{L}$ , and  $100 \mu\text{L}$  of electrolyte, b) CE comparison using the conventional method at  $1.0 \text{ mA cm}^{-2}$  in coin cell, c) voltage profile variation before and after injection of electrolyte, d) cycling and CE performance of the cell before and after injection of electrolyte, e) Effect of adding electrolyte on voltage polarization of the cell before and after injection of electrolyte, and f) voltage profile comparison between  $50 \mu\text{L}$  and  $100 \mu\text{L}$  using reservoir method at  $1.0 \text{ mA cm}^{-2}$ .

Then, the conventional method is used to verify the effect of ZnO thickness on lithium metal cycling at a current density of  $1 \text{ mA cm}^{-2}$  and capacity of  $1 \text{ mAh cm}^{-2}$ , as shown in Fig. 4c. An identical behavior is observed for all thicknesses, a decrease of the CE followed by an increase and a stabilization/fluctuation until a decrease of the reversible capacity, the sign of the battery failure. Currently, for the ZnO samples, the reason behind the CE increasing in the initial cycles of the experiment and its following decrease is unclear. In addition, with an increase in deposit ZnO thickness, the CE fluctuates more. Possibly, it is caused by isolated lithium that can be reconnected in a subsequent plating/stripping cycle when lithium is deposited homogeneously<sup>38,59</sup>.

Regarding performance, even though the average CE of uncoated Ni foam looks better than that of ZnO-modified samples when the common method is used, the latter samples exhibit much better cycling stability for all ZnO coating thicknesses. The best cycle life is obtained with a ZnO layer thickness between 10 nm and 50 nm; indeed, these samples show stable cycling up to about 190 cycles before fading. In contrast, with the reservoir method, both cycling stability and calculated average CE improve while increasing the ZnO layer thickness (Fig. 4d and e).

The different results obtained with conventional and reservoir methods make it quite challenging to accurately determine the optimal thickness of ZnO. The conventional method can provide cycle-by-cycle efficiency; however, in the following section, we will demonstrate that the cycling performance of the cells determined with it is also tremendously dependent on the volume of electrolyte. Moreover, this method is not reflective of practical LMBs since these typically contain excess Li. Accordingly, the conventional plating and stripping method can be more effectively used in AFBs systems or for screening different electrolytes at

low potentials. On the other hand, the reservoir method with partial plating and stripping leaves a layer of lithium reservoir after the first cycle, comparable to what is typically operated in practical LMBs. This method, however, does not consider the loss of lithium during the first cycle thus providing a more accurate estimation of the average CE for LMBs. It is particularly important to consider the loss of lithium during the first cycle in AFBs where the lithium coming from the cathode is limited. According to the reservoir method results, the 100 nm and 150 nm layer modified ZnO are promising. Nevertheless, they have a first cycle CE of 78.2% and 68.4%, respectively, making questionable their practical application in AFBs. Hence, the lower thickness of the ZnO causes reduced loss of lithium during the first cycle of the conversion/alloying process, which could be more useful for AFBs. On the other hand, given the substantial excess of lithium in LMBs, the samples with a thicker layer of ZnO would be more suitable for use as a host to infuse molten Li.

### Influence of electrolyte amount

The amount of electrolyte also significantly impacts the CE and cycling performance of LMBs and AFBs<sup>39,41</sup>. Half-cell Li||Ni batteries containing  $50 \mu\text{L}$ ,  $75 \mu\text{L}$ , and  $100 \mu\text{L}$  electrolytes were prepared to verify the influence of the amount of electrolyte on the cyclability. As shown in Fig. 5a, a larger amount of electrolyte results in a longer pre-cycling procedure. The increased amount of electrolyte on the surface may thus cause the degradation of the larger amount of electrolyte and the formation of a thicker SEI during activation. Using the conventional method, cycling stability is evaluated after the stabilization process, as shown in Fig. 5b. These results show that a larger volume of the electrolyte leads to an increase in cell lifetime. By doubling the

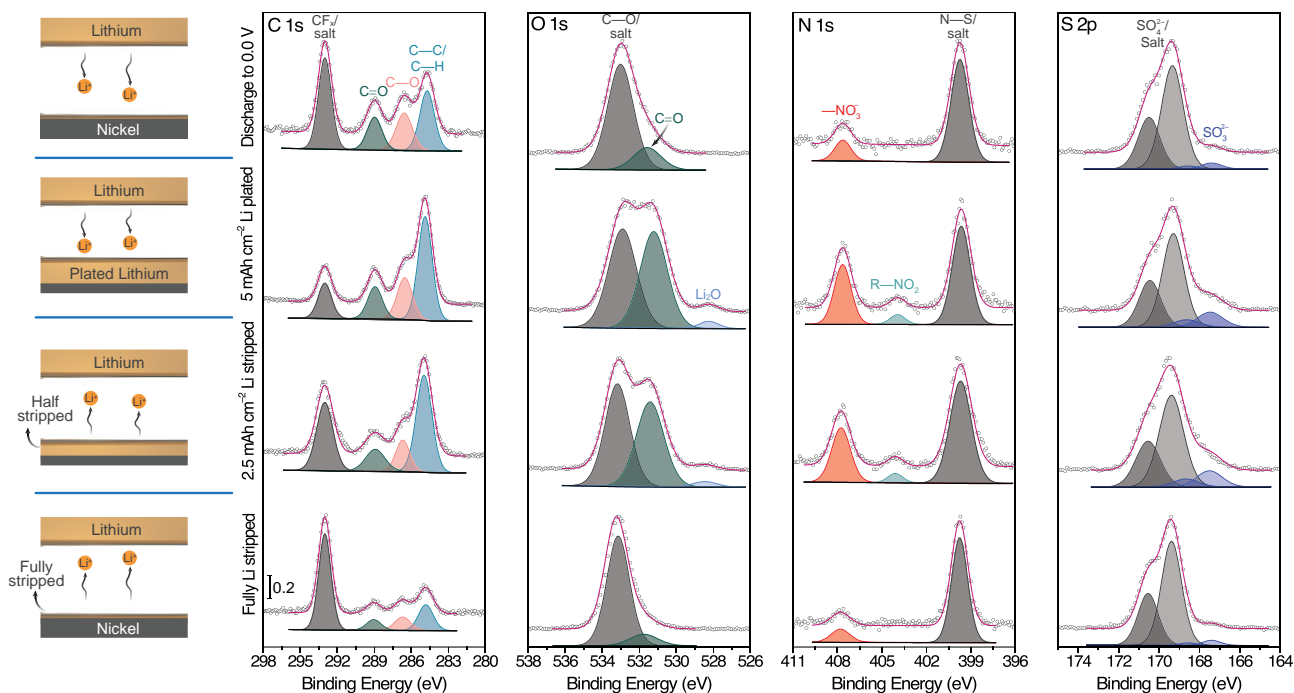


**Fig. 6: XPS characterization to identify the mechanism of cell failure:** XPS spectra of C 1s, O 1s, N 1s, and S 2p for SEI layers in different stages of plating/stripping, SEI formation (discharge the battery to 0.0 V), lithium plated on the Ni foam, stripping half of the plated lithium (represent the reservoir method), and stripping all the lithium on the surface (represent the conventional method).

amount of electrolyte, the number of cycles doubles. On the other hand, the batteries opened and inspected after cycling were completely dry. Continuous electrolyte loss due to the formation and continuous growth of SEI layers, as well as high surface area or dead lithium formation<sup>80</sup>, leads to battery failure.

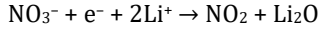
Additionally, a two-electrode Swagelok Li||Ni cell was used to investigate the effect of electrolyte amount on cyclic stability. As shown in Fig. 5c-d, long-term cycling leads to a progressive increase in polarization and a parallel gradual decrease in CE of the half-cell. Before the complete failure, the cell was opened and refilled with 100  $\mu$ L of fresh electrolyte. This refilling leads to a decrease in polarization and complete recovery of the previous lithium plating/stripping conditions (black curve in Fig. 5c and e). The addition of 100  $\mu$ L of electrolyte induces an immediate increase in CE (black scatters Fig. 5d). These results clearly show that not only the electrolyte amount plays a significant role in cycling stability but also that electrolyte consumption is the main cause of failure in a conventional electrochemical test. These results are coherent with recent reports by Li et al.<sup>80</sup> and Xiao et al.<sup>39</sup>. As a comparison, the same analysis was conducted with the reservoir method (Fig. 5f). In this case, the failure results are independent of the amount of electrolyte. Despite the reduced electrolyte volume, cell failure was not affected, indicating that the mechanism of cell failure is regardless of the amount of electrolyte. If a dominant failure mode can be identified through diagnostic testing, it allows an accurate estimation of cycle life and CE for LMBs and AFBs<sup>81</sup>. The mechanism behind cell failure in this case will be studied in the following section (*vide infra*).

## Mechanism of cell failure

It is well known that the SEI layer plays a critical role in the electrochemical behaviors of batteries<sup>82-85</sup> as the instability of the SEI is the main cause of electrolyte depletion. To further clarify and understand the reason for electrolyte depletion during electrochemical lithium plating/stripping with both conventional and reservoir methods, XPS was used to analyze the SEI layer formed on Ni foam at various stages of plating/stripping cycles (Fig. S7a) including preliminary SEI (discharge to 0.0 V), plated Li, stripped half of the plated lithium (the reservoir method), and fully stripped sample (the conventional method). In general, the SEI layers are composed of relatively enriched inorganic species in the inner part close to the lithium metal surface and a higher content of an organic layer with polymeric species in the outer part close to the electrolyte<sup>86,87</sup>. The inorganic part of the SEI layer originates mainly from the decomposition products of electrolyte lithium salts and additive and/or residual salts trapped in the SEI layer, i.e., LiTFSI and LiNO<sub>3</sub>, while the organic species of the SEI layer are assumed to form via the decomposition and polymerization products of the solvent<sup>88,89</sup>, i.e., DOL and DME. As shown in Fig. 6, the C 1s XPS spectra display several characteristic peaks of the components of the polymeric surface layer. All show strong characteristic salt peaks at 293 eV corresponding to the -CF<sub>x</sub> group, which originates from either pristine LiTFSI salts or incomplete salt decomposition (Li<sub>2</sub>NSO<sub>2</sub>CF<sub>3</sub>, LiSO<sub>2</sub>CF<sub>3</sub>, and Li<sub>y</sub>C<sub>2</sub>F<sub>x</sub>)<sup>90-92</sup>. These compounds show characteristic peaks at 533 eV in the O 1s, 399.6 eV in the N 1s, and 169.3 eV in the S 2p<sub>3/2</sub><sup>23</sup>. Further reduction of these compounds results in inorganic compounds such as Li<sub>3</sub>N, LiF, Li<sub>2</sub>S<sub>2</sub>O<sub>4</sub>, Li<sub>2</sub>S, Li<sub>x</sub>S<sub>y</sub>O<sub>z</sub>, LiCF<sub>3</sub>, and Li<sub>x</sub>C<sub>2</sub>F<sub>y</sub><sup>90,92,93</sup>. The peaks at 284.8 and 286.5 eV are attributed to aliphatic hydrocarbons and to C-

O species, respectively<sup>94,95</sup>. Further, the peak at 289 eV originates from carbonate species such as lithium carbonate ( $\text{Li}_2\text{CO}_3$ ), lithium alkyl carbonates ( $\text{ROCO}_2\text{Li}$ ), and semi-carbonated species such as  $(\text{CH}_2\text{OCO}_2\text{Li})_2$  and/or polymeric species of poly-DOL<sup>88,95,96</sup>. The SEI layer contains organic compounds formed by the reduction of DOL and DME<sup>93</sup>. Upon stripping half of the plated lithium metal, there is a slight decrease in the organic-inorganic compounds. While the stripping is completed and all the metallic lithium has been removed, similar to the conventional electrochemical method, the intensity peaks of both organic-inorganic layers sharply decrease, suggesting that part of the SEI may have dissolved.

The O 1s spectrum exhibits two peaks at 533 and 531.5 eV corresponding to C-O/salt and C=O (i.e.,  $\text{Li}_2\text{CO}_3$ ,  $(\text{CH}_2\text{OCO}_2\text{Li})_2$ , and  $\text{ROCO}_2\text{Li}$ ), respectively<sup>23,88,97</sup>. The C=O peak has a distinct intensity between the Li-plated and totally stripped samples, suggesting that electrolyte (salt/solvent) contributes more to SEI composition during plating and/or that part of the SEI is dissolved/removed during stripping. Additionally, the samples with lithium plated on the surface displayed a  $\text{Li}_2\text{O}$  peak at 528.4 eV derived from the  $\text{LiNO}_3$  decomposition, in accordance with the previous report<sup>92</sup>:



In addition to LiTFSI,  $\text{LiNO}_3$  also contributes to forming the SEI layer<sup>23</sup>. Regarding the N 1s spectra for the native SEI sample, two peaks at 399.6 and 407.6 eV can be assigned to nitrogen in the N-S (salt) bond and  $-\text{NO}_3^-$ , respectively<sup>23,90,91</sup>. The lithium plated samples presented an additional peak around the 404 eV which is assigned to functional nitro groups R- $\text{NO}_2$  (R=organic) or nitrite ( $\text{NO}_2^-$ ) compounds, suggesting that  $\text{LiNO}_3$  is reduced to  $\text{NO}_2$  radical and initiates a polymeric reaction with DOL to form organic nitro (R- $\text{NO}_2$ ) compounds<sup>92</sup>. Therefore,  $\text{LiNO}_3$ , as well as other electrolyte components, undergoes decomposition during plating and stripping. Two distinct species can be identified in the S 2p spectra. The peak around 169.3 eV is attributed to sulfonyl groups  $-\text{SO}_2\text{CF}_3$  from the pristine salt or its incomplete decomposition products. Also, the peak around 167.4 eV belongs to sulfonyl residuals with stripped fluorine  $-\text{SO}_2\text{CF}_2^+$  or  $\text{Li}_x\text{SO}_y$ <sup>93,95,98</sup>. The S 2p spectra exhibit a similar pattern to those of C 1s, O 1s, and N 1s during the plating and stripping of Li.

Overall, the differences between the C 1s, O 1s, N 1s, and S 2p spectra of the plated and stripped lithium samples are clear and pronounced. As illustrated in Fig. 7, SEI continuously grows during the deposition of  $\text{Li}^0$  and remains unchanged during the half-stripping of the  $\text{Li}^0$  (as in the reservoir method). When lithium metal is completely stripped from the substrate (the same procedure as the conventional electrochemical method), on the contrary, the content of organic-inorganic compounds within the SEI layer significantly reduces. It seems reasonable to assume that some SEI parts dissolve while lithium is entirely stripped from the electrode surface. The electrolyte depletion for the conventional electrochemical method is connected to the evolution (destruction/reconstitution) of the SEI during the lithium

plating and stripping for each cycle. In this manner, the remaining portion of  $\text{Li}^0$  on the surface may mitigate electrolyte decomposition (similar to the reservoir method).

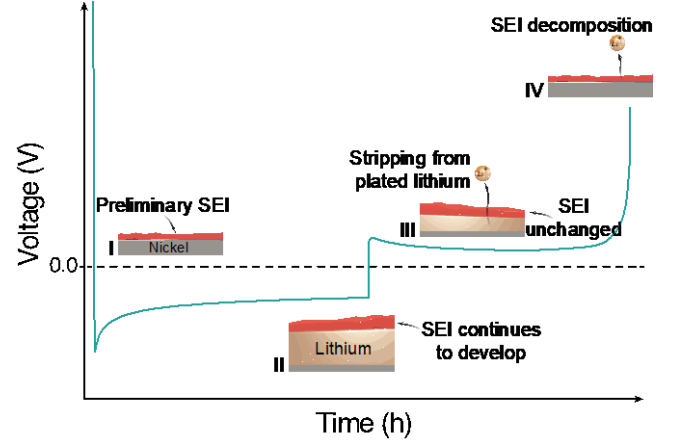


Fig. 7: **The SEI evolution during plating and stripping of Li:** I) preliminary SEI formed on the surface of Ni foam, II) during the plating, SEI continuously grows, III) during half-stripping, the SEI remains unchanged, and IV) fully stripping of lithium leads to SEI dissolution.

### Evolution of the SEI in AFBs

To further elucidate the behavior of the SEI during the complete stripping of plated lithium, anode-free cells were investigated using Ni current collector as the anode and commercial  $\text{LiFePO}_4$  (LFP) electrodes as the cathode. Such systems contain a limited source of lithium ions generated from the LFP cathode, and therefore any inefficiency in lithium plating-stripping can be quickly detected. As illustrated in Fig. 8a, Li-ions are de-intercalated from the LFP electrode and plated onto the Ni foam when the anode-free cell is fully charged. In reverse, during the discharge of the cell, Li-ions are intercalated back into the LFP electrode. All batteries were first submitted to a full charge/discharge cycle at a constant current of  $0.1 \text{ mA cm}^{-2}$  within a potential range of 2.5–4.2 V. For the subsequent cycles, the upper cutoff voltage was constantly set at 4.2 V while different lower cutoff voltages were used to evaluate the SEI dissolution. In the first protocol, the lower cutoff voltage was set at 2.5 V, indicating that all the removable lithium has been stripped from the anode electrode surface (similar to the conventional method). The galvanostatic cycling curves with the corresponding CE and capacity retention are shown in Fig. 8c and 8b, respectively. In the reservoir method (Fig. 8d), after extracting all the Li-ions from the LFP and plated to the Ni surface, the batteries were cycled with a limited stripping capacity ( $1.0 \text{ mAh cm}^{-2}$ ,  $Q_c$ ) rather than to a constant lower cutoff voltage. Extra active lithium metal remaining on the anode surface ( $Q_r$ ) serves as a lithium reservoir in the subsequent cycles and supplies active lithium for consumption by the side reactions in the subsequent cycles. After  $n$  cycles, the reservoir lithium on the substrate is completely consumed, which is visible by decreases in the lower cutoff voltage to 2.5 V. The average CE over  $n$  cycles can be calculated by using Eq. 2. In addition, for the first protocol, the average CE can be calculated according to Eq. 3:

$$CE_{avg} = \frac{1}{n-1} \sum_{k=2}^n \frac{\text{Stripping capacity}}{\text{Plating capacity}} \times 100\% \quad \text{Eq. 3}$$

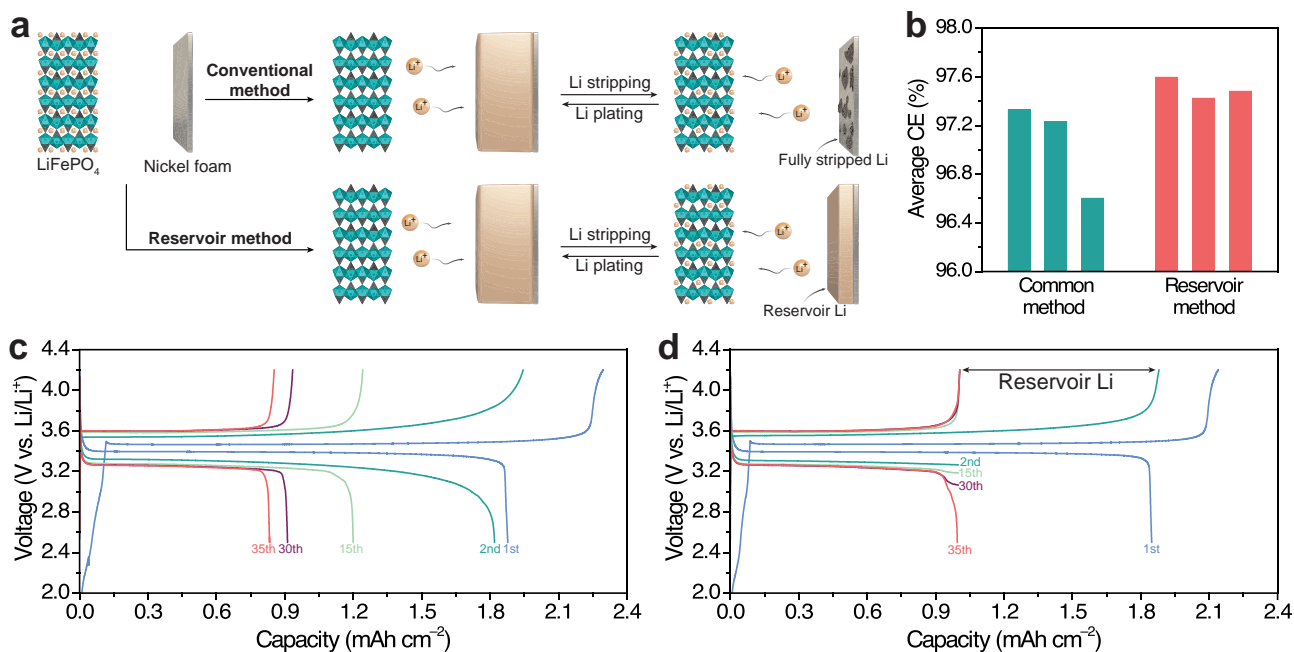


Fig. 8: **Evolution of the SEI in anode-free Ni||LFP cell:** a) schematic illustration of conventional and reservoir methods, b) average CE calculated for conventional and reservoir methods (three identical samples were measured, and each bar represents a single cell), and charge/discharge voltage profile selection in conventional (c) and reservoir (d) method, when current density at the first cycle was at  $0.1 \text{ mA cm}^{-2}$  and for the following cycles were under  $0.5 \text{ mA cm}^{-2}$ ; in reservoir method, once the voltage drop to 2.5 V (35th cycle) the reservoir has consumed its entire capacity.

It is noted that the CE of the first cycle is not included in the calculations for both protocols. As shown in Fig. 8b, the average CE of the reservoir method is found to be higher compared to the conventional method. This lower CE for the conventional method could be ascribed to the fact that the continuous formation/repair of the SEI layer induces higher Li consumption, which is in limited amounts in the cathode. Conversely, by keeping some metallic lithium on the anode electrode, the SEI is better preserved during cycling, leading to a higher CE. This finding is in line with previous reports<sup>99,100</sup> and the results shown in the aforementioned sections for common and reservoir methods, clearly indicating how it may be possible to improve the CE of AFBs in practical application.

## CONCLUSIONS

Two different electrochemical methods were utilized in this study to highlight the effect of different experimental factors, which are often neglected in many studies, on the measurement of CE and cycling performance of LMBs/AFBs. Hidden and inconspicuous electrochemical and cell parameters can substantially affect the performance of the benchmark system. As a result of the findings in this paper, several key points were clarified:

**Cutoff:** Despite the fact that the average CE decreases by lowering the upper cutoff potential in the conventional electrochemical method, the cycle life can be extended. In other words, increased high cutoff potentials lead to reduced lifespan due to the further decomposition of electrolytes and irreversible electrochemical reactions. Accordingly, the lower cutoff voltage is recommended for lithium plating and stripping tests.

**Pre-cycling for initial SEI formation:** Galvanostatic pre-cycling to form and stabilize SEI is here shown to not affect the cycling performance and CE measurements for the conventional electrochemical method. Most probably, the stabilized SEI can be easily changed and damaged by the complete stripping of lithium and the continued plating of Li. However, in the reservoir method, stabilizing the SEI via pre-cycling before lithium deposition improved CE values. Due to the initial SEI formation, the nucleation overpotential of the electrode increases; this allows the unveiling of the hidden aspects of the nucleation overpotential of the batteries.

**Nucleation overpotential:** The results from three-electrode cells indicate that the energy barrier for stripping or extracting lithium from the lithium metal counter electrode is significantly higher than the energy barrier for forming nucleation sites on the working electrode when the cell starts cycling. This also explains why the pre-cycling to form initial SEI induced a higher nucleation overpotential.

**Modification of electrode surface:** The optimal thickness of ZnO coating on the Ni foam current collector was shown to be below 50 nm when using the conventional method, whereas increasing the thickness improves the performance in the reservoir method. The results indicate that the lower thickness of ZnO would be more suitable for use in AFBs with a limited source of lithium in the cathode electrode, whereas a higher thickness of ZnO would be more beneficial for infusing molten lithium to use as an anode in the LMBs. In general, it is challenging to determine the effective optimal thickness of coatings in modified materials.

**Quantity of electrolyte:** In the conventional electrochemical method, the mechanism of cell failure is electrolyte depletion rather than dendrite formation, and the cycle life of a battery is directly proportional to its electrolyte volume. In contrast, the reservoir method shows that the failure is independent of the amount of electrolyte. Furthermore, XPS analysis reveals that the evolution of SEI during lithium plating and the entire stripping of lithium for each cycle leads to electrolyte depletion in the conventional electrochemical method.

**SEI in AFBs:** The results for AFBs show similar that the cycled life could be improved by keeping some metallic lithium on the anode electrode, resulting in higher stability of the SEI and thus higher CE values.

We believe that by gathering this type of information, researchers may be able to gain a deeper understanding of the efficiency of different parameters but also of different analytical methods in the thorough understanding of lithium plating and stripping processes.

## EXPERIMENTAL SECTION

**Materials.** Diethyl zinc (DEZ), 1,2-dimethoxyethane (DME), 1,3-dioxolane (DOL), lithium nitrate ( $\text{LiNO}_3$ ), Bis(trifluoromethylsulfonyl)amine lithium salt (LiTFSI), and Li metal foil (350  $\mu\text{m}$  thick) were all purchased from Sigma. The lithium iron phosphate (LFP) on Al foil with a capacity of 2.0 mAh  $\text{cm}^{-2}$  was purchased from Lifesize company in Sweden. Nickel (Ni) foam with a thickness of 300  $\mu\text{m}$ , > 0.1 g  $\text{cm}^{-3}$  volume density, > 99% purity and 95-98 % porosity was purchased from TMAX company in China. All other chemicals used in this work were of analytical reagent grade and were used without further purification.

**Material synthesis.** An atomic layer deposition (ALD) process was used to modify the surface of Ni foam with lithiophilic zinc oxide (ZnO) materials with different thicknesses. The deposition was carried out in a home-built reactor at 100 °C with DEZ and milli-Q water as precursors and co-reactants, respectively. Precursors were maintained at room temperature, and the lines connected to the chamber were heated at 80 °C to prevent condensation. A typical ALD sequence was applied with a 0.4 s pulse of DEZ and a 2 s pulse of water. Each pulse was exposed for 30 seconds and purged for 40 seconds using Argon between pulses. The different thickness of ZnO was depicted by varying the number of ALD cycles from 50 to 500 cycles.

**Electrochemical measurements.** Electrochemical measurements were performed in CR2032 coin-type cells assembled in an argon-filled glovebox (MBraun) with less than one ppm  $\text{O}_2$  and  $\text{H}_2\text{O}$ . The electrolyte used in this paper consisted of 1M LiTFSI in DOL / DME (1/1 volume ratio) with 2 wt% of  $\text{LiNO}_3$ . A piece of Celgard 2325 was used as a separator. The pure Ni or ZnO coated foam (1.27 cm  $\emptyset$ ) was used as a working electrode, whereas the reference/counter electrode was a piece of Li metal foil. The data was collected using the potentiostat capabilities of the Biologic MPG-2 system at  $25 \pm 2$  °C. The assembled cells were pre-cycled between 0.01 and 1 V at 0.2 mA  $\text{cm}^{-2}$  five times to make the SEI stabilization procedure. For the full cell AFBs analysis, the cells were first cycled at a mild constant current condition at 0.1 mA  $\text{cm}^{-2}$  for the first cycle within a potential range of 2.5–4.2 V; the following cycles were performed at

the current density of 0.5 mA  $\text{cm}^{-2}$ . Three-electrode measurements were performed to decouple the potential contributions from Li and Ni foam electrodes in order to study the nucleation overpotential. Two pieces of Celgard 2325 as the separator and 1.0 mL of electrolyte were used for the Swagelok cells. The non- or ZnO-coated Ni foam (0.95 mm  $\emptyset$ ) were used as a working electrode, whereas two pieces of Li metal foil (10 mm  $\emptyset$  and 750  $\mu\text{m}$  thick, Alfa Aesar) were used as the reference and the counter electrode.

**Characterizations.** The XPS results were obtained from the coin cell to investigate the plating and different stages of Li stripping on the SEI with the constant current density of 0.5 mA  $\text{cm}^{-2}$ . The samples were rinsed by immersion in DME, and the residual DME was removed by drying in the Ar glovebox prior to XPS analysis. The samples were transferred to an XPS chamber using a vacuum transfer vessel. The XPS measurements were taken using PHI 5500® and Kratos Axis Supra and spectrometers equipped with a monochromatic Al  $K\alpha$  radiation (1487 eV) source. The binding energy was calibrated to the  $-\text{CF}_x$  peak in the C 1s spectra (293.0 eV). Data were analyzed with the CasaXPS package software, employing the Gaussian-Lorentzian peak shape GL(30).

## ASSOCIATED CONTENT

Supporting Information is available: Figures S1–S7.

## AUTHOR INFORMATION

### Corresponding Author

Lorenzo Stievano

Email address:

[Lorenzo.stievano@umontpellier.fr](mailto:Lorenzo.stievano@umontpellier.fr)

### Funding Sources

The authors gratefully acknowledge financial support from the French National Research Agency (project Labex STORE-EX, ANR-10-LABX-76-01) and the Swedish Energy Agency via StandUp for Energy.

### Notes

The authors declare that they have no known competing financial interests or personal relationships that could have appeared to influence the work reported in this paper.

## ACKNOWLEDGMENT

The Alistore-European Research Institute (ALISTORE-ERI) network is warmly thanked for funding the Ph.D. grant of A. M.

## ABBREVIATIONS

LMBs, lithium metal batteries; CE, coulombic efficiency; AFBs, anode-free lithium metal batteries; ZnO, zinc oxide; 3D, three-dimensional.

## REFERENCES

1. Fichtner, M. *et al.* Rechargeable Batteries of the Future—The State of the Art from a BATTERY 2030+ Perspective. *Adv. Energy Mater.* **12**, 2102904 (2022).
2. He, X. *et al.* The passivity of lithium electrodes in liquid electrolytes for secondary batteries. *Nat. Rev. Mater.* **6**, 1036–1052 (2021).
3. Zou, P. *et al.* Polymorph Evolution Mechanisms and Regulation Strategies of Lithium Metal Anode under Multiphysical Fields. *Chem. Rev.* **121**, 5986–6056 (2021).

4. Horstmann, B. *et al.* Strategies towards enabling lithium metal in batteries: interphases and electrodes. *Energy Environ. Sci.* **14**, 5289–5314 (2021).
5. Foroozan, T., Sharifi-Asl, S. & Shahbazian-Yassar, R. Mechanistic understanding of Li dendrites growth by in-situ/operando imaging techniques. *J. Power Sources* **461**, 228135 (2020).
6. Cheng, X. B., Zhang, R., Zhao, C. Z. & Zhang, Q. Toward Safe Lithium Metal Anode in Rechargeable Batteries: A Review. *Chem. Rev.* **117**, 10403–10473 (2017).
7. Wood, K. N., Noked, M. & Dasgupta, N. P. Lithium metal anodes: Toward an improved understanding of coupled morphological, electrochemical, and mechanical behavior. *ACS Energy Lett.* **2**, 664–672 (2017).
8. Qian, J. *et al.* Anode-Free Rechargeable Lithium Metal Batteries. *Adv. Funct. Mater.* **26**, 7094–7102 (2016).
9. Su, L., Charalambous, H., Cui, Z. & Manthiram, A. High-efficiency, anode-free lithium-metal batteries with a close-packed homogeneous lithium morphology. *Energy Environ. Sci.* **15**, 843–854 (2022).
10. Lin, L. *et al.* A Better Choice to Achieve High Volumetric Energy Density: Anode-Free Lithium-Metal Batteries. *Adv. Mater.* **34**, 2110323 (2022).
11. Louli, A. J. *et al.* Different Positive Electrodes for Anode-Free Lithium Metal Cells. *J. Electrochem. Soc.* **169**, 040517 (2022).
12. Kushima, A. *et al.* Liquid cell transmission electron microscopy observation of lithium metal growth and dissolution: Root growth, dead lithium and lithium flotsams. *Nano Energy* **32**, 271–279 (2017).
13. Huang, C. J. *et al.* Decoupling the origins of irreversible coulombic efficiency in anode-free lithium metal batteries. *Nat. Commun.* **12**, 1452 (2021).
14. Tong, Z., Bazri, B., Hu, S. F. & Liu, R. S. Interfacial chemistry in anode-free batteries: challenges and strategies. *J. Mater. Chem. A* **9**, 7396–7406 (2021).
15. Zhou, M. Y. *et al.* Quantifying the apparent electron transfer number of electrolyte decomposition reactions in anode-free batteries. *Joule* 1–16 (2022). doi:10.1016/j.joule.2022.07.003
16. Wood, K. N. *et al.* Dendrites and Pits: Untangling the Complex Behavior of Lithium Metal Anodes through Operando Video Microscopy. *ACS Cent. Sci.* **2**, 790–801 (2016).
17. Xu, Y. *et al.* Promoting Mechanistic Understanding of Lithium Deposition and Solid-Electrolyte Interphase (SEI) Formation Using Advanced Characterization and Simulation Methods: Recent Progress, Limitations, and Future Perspectives. *Adv. Energy Mater.* **12**, 2200398 (2022).
18. Bai, P., Li, J., Brushett, F. R. & Bazant, M. Z. Transition of lithium growth mechanisms in liquid electrolytes. *Energy Environ. Sci.* **9**, 3221–3229 (2016).
19. Liu, F. *et al.* Dynamic spatial progression of isolated lithium during battery operations. *Nature* **600**, 659–663 (2021).
20. Hobold, G. M. *et al.* Moving beyond 99.9% Coulombic efficiency for lithium anodes in liquid electrolytes. *Nat. Energy* **6**, 951–960 (2021).
21. Younesi, R., Veith, G. M., Johansson, P., Edström, K. & Vegge, T. Lithium salts for advanced lithium batteries: Li-metal, Li-O<sub>2</sub>, and Li-S. *Energy Environ. Sci.* **8**, 1905–1922 (2015).
22. Huang, C.-J. *et al.* Lithium Oxalate as a Lifespan Extender for Anode-Free Lithium Metal Batteries. *ACS Appl. Mater. Interfaces* **14**, 26724–26732 (2022).
23. Kang, D. W., Moon, J., Choi, H.-Y., Shin, H.-C. & Kim, B. G. Stable cycling and uniform lithium deposition in anode-free lithium-metal batteries enabled by a high-concentration dual-salt electrolyte with high LiNO<sub>3</sub> content. *J. Power Sources* **490**, 229504 (2021).
24. Kim, M. S. *et al.* Suspension electrolyte with modified Li+ solvation environment for lithium metal batteries. *Nat. Mater.* **21**, 445–454 (2022).
25. Wang, D. *et al.* Synchronous Healing of Li Metal Anode via Asymmetrical Bidirectional Current. *iScience* **23**, 100781 (2020).
26. Wang, X. *et al.* Inhibiting Dendrite Growth via Regulating the Electrified Interface for Fast-Charging Lithium Metal Anode. *ACS Cent. Sci.* **7**, 2029–2038 (2021).
27. Huang, Y., Pan, R., Rehnlund, D., Wang, Z. & Nyholm, L. First-Cycle Oxidative Generation of Lithium Nucleation Sites Stabilizes Lithium-Metal Electrodes. *Adv. Energy Mater.* **11**, 2003674 (2021).
28. Touja, J., Louvain, N., Stievano, L., Monconduit, L. & Berthelot, R. An Overview on Protecting Metal Anodes with Alloy-Type Coating. *Batter. Supercaps* **4**, 1252–1266 (2021).
29. Hagopian, A. *et al.* Importance of Halide Ions in the Stabilization of Hybrid Sn-Based Coatings for Lithium Electrodes. *ACS Appl. Mater. Interfaces* **14**, 10319–10326 (2022).
30. Chen, W. *et al.* Brushed Metals for Rechargeable Metal Batteries. *Adv. Mater.* **34**, 2202668 (2022).
31. Li, S. *et al.* A robust all-organic protective layer towards ultrahigh-rate and large-capacity Li metal anodes. *Nat. Nanotechnol.* **17**, 613–621 (2022).
32. Duan, C. *et al.* Realizing the compatibility of a Li metal anode in an all-solid-state Li-S battery by chemical iodine-vapor deposition. *Energy Environ. Sci.* **15**, 3236–3245 (2022).
33. Roitzheim, C. *et al.* All-Solid-State Li Batteries with NCM-Garnet-Based Composite Cathodes: The Impact of NCM Composition on Material Compatibility. *ACS Appl. Energy Mater.* **5**, 6913–6926 (2022).
34. Huang, W. *et al.* Anode-Free Solid-State Lithium Batteries: A Review. *Adv. Energy Mater.* **12**, 2201044 (2022).
35. Han, K. H. *et al.* A 2D Ultrathin Nanopatterned Interlayer to Suppress Lithium Dendrite Growth in High-Energy Lithium-Metal Anodes. *Adv. Mater.* **34**, 2203992 (2022).
36. Yun, J., Won, E.-S., Shin, H.-S., Jung, K.-N. & Lee, J.-W. Efficient and robust lithium metal electrodes enabled by synergistic surface activation-passivation of copper frameworks. *J. Mater. Chem. A* **7**, 23208–23215 (2019).
37. Liu, H. *et al.* An anode-free Li metal cell with replenishable Li designed for long cycle life. *Energy Storage Mater.* **36**, 251–256 (2021).
38. Zheng, J. *et al.* Physical Orphaning versus Chemical Instability: Is Dendritic Electrodeposition of Li Fatal? *ACS Energy Lett.* **4**, 1349–1355 (2019).
39. Xiao, J. *et al.* Understanding and applying coulombic efficiency in lithium metal batteries. *Nat. Energy* **5**, 561–568 (2020).
40. Smith, A. J., Burns, J. C., Trussler, S. & Dahn, J. R. Precision Measurements of the Coulombic Efficiency of Lithium-Ion Batteries and of Electrode Materials for Lithium-Ion Batteries. *J. Electrochem. Soc.* **157**, A196 (2010).
41. Winter, E., Schmidt, T. J. & Trabesinger, S. Identifying Pitfalls in Lithium Metal Battery Characterization. *Batter. Supercaps* **5**, e202100145 (2022).
42. Adams, B. D., Zheng, J., Ren, X., Xu, W. & Zhang, J. Accurate Determination of Coulombic Efficiency for Lithium Metal Anodes and Lithium Metal Batteries. *Adv. Energy Mater.* **8**, 1702097 (2018).
43. Aurbach, D., Youngman, O. & Dan, P. The electrochemical behavior of 1,3-dioxolane-LiClO<sub>4</sub> solutions-II. Contaminated solutions. *Electrochim. Acta* **35**, 639–655 (1990).
44. Lin, L. *et al.* Epitaxial Induced Plating Current-Collector Lasting Lifespan of Anode-Free Lithium Metal Battery. *Adv. Energy Mater.* **11**, 2003709 (2021).
45. Chen, Y. *et al.* Steric Effect Tuned Ion Solvation Enabling Stable Cycling of High-Voltage Lithium Metal Battery. *J. Am. Chem. Soc.* **143**, 18703–18713 (2021).
46. Qiu, F. *et al.* A Concentrated Ternary-Salts Electrolyte for High Reversible Li Metal Battery with Slight Excess Li. *Adv. Energy Mater.* **9**, 1803372 (2019).
47. Xu, R. *et al.* Designing and Demystifying the Lithium Metal Interface toward Highly Reversible Batteries. *Adv. Mater.* **33**, 2105962 (2021).
48. Wang, H. *et al.* Dual-Solvent Li-Ion Solvation Enables High-Performance Li-Metal Batteries. *Adv. Mater.* **33**, 2008619 (2021).
49. Wu, J. *et al.* Gradient Design for High-Energy and High-Power Batteries. *Adv. Mater.* **34**, 2202780 (2022).
50. Lyu, T. *et al.* Carbon/Lithium Composite Anode for Advanced Lithium Metal Batteries: Design, Progress, In Situ Characterization, and Perspectives. *Adv. Energy Mater.*

- 2201493 (2022). doi:10.1002/aenm.202201493
51. Chen, K.-H., Sanchez, A. J., Kazayak, E., Davis, A. L. & Dasgupta, N. P. Synergistic Effect of 3D Current Collectors and ALD Surface Modification for High Coulombic Efficiency Lithium Metal Anodes. *Adv. Energy Mater.* **9**, 1802534 (2019).
52. Li, T. *et al.* Bidirectional Lithiophilic Gradients Modification of Ultralight 3D Carbon Nanofiber Host for Stable Lithium Metal Anode. *Small* **18**, 2203273 (2022).
53. Xu, N., Li, L., He, Y., Tong, Y. & Lu, Y. Understanding the molecular mechanism of lithium deposition for practical high-energy lithium-metal batteries. *J. Mater. Chem. A* **8**, 6229–6237 (2020).
54. Adams, B. D. *et al.* Long term stability of Li-S batteries using high concentration lithium nitrate electrolytes. *Nano Energy* **40**, 607–617 (2017).
55. Wang, J. *et al.* Improving cyclability of Li metal batteries at elevated temperatures and its origin revealed by cryo-electron microscopy. *Nat. Energy* **4**, 664–670 (2019).
56. Dose, W. M., Xu, C., Grey, C. P. & De Volder, M. F. L. Effect of Anode Slippage on Cathode Cutoff Potential and Degradation Mechanisms in Ni-Rich Li-Ion Batteries. *Cell Reports Phys. Sci.* **1**, 100253 (2020).
57. Liu, Y. *et al.* The Impact of Upper Cut-Off Voltage on the Cycling Performance of Li-Ion Cells with Positive Electrodes Having Various Nickel Contents. *J. Electrochem. Soc.* **169**, 040531 (2022).
58. Zhang, S. S. Effect of Discharge Cutoff Voltage on Reversibility of Lithium/Sulfur Batteries with LiNO<sub>3</sub>-Contained Electrolyte. *J. Electrochem. Soc.* **159**, A920–A923 (2012).
59. Wang, H. *et al.* Improving Lithium Metal Composite Anodes with Seeding and Pillaring Effects of Silicon Nanoparticles. *ACS Nano* **14**, 4601–4608 (2020).
60. Tang, S. *et al.* Stable Na Plating and Stripping Electrochemistry Promoted by In Situ Construction of an Alloy-Based Sodiophilic Interphase. *Adv. Mater.* **31**, 1807495 (2019).
61. Zhang, S. *et al.* Phase Diagram Determined Lithium Plating/Stripping Behaviors on Lithiophilic Substrates. *ACS Energy Lett.* **6**, 4118–4126 (2021).
62. Jin, S. *et al.* Solid-Solution-Based Metal Alloy Phase for Highly Reversible Lithium Metal Anode. *J. Am. Chem. Soc.* **142**, 8818–8826 (2020).
63. Zheng, G. *et al.* Interconnected hollow carbon nanospheres for stable lithium metal anodes. *Nat. Nanotechnol.* **9**, 618–623 (2014).
64. Evmenenko, G. *et al.* Morphological Evolution of Multilayer Ni/NiO Thin Film Electrodes during Lithiation. *ACS Appl. Mater. Interfaces* **8**, 19979–19986 (2016).
65. Kushima, A. *et al.* Leapfrog Cracking and Nanoamorphization of ZnO Nanowires during In Situ Electrochemical Lithiation. *Nano Lett.* **11**, 4535–4541 (2011).
66. Yan, K. *et al.* Selective deposition and stable encapsulation of lithium through heterogeneous seeded growth. *Nat. Energy* **1**, 16010 (2016).
67. Pei, A., Zheng, G., Shi, F., Li, Y. & Cui, Y. Nanoscale Nucleation and Growth of Electrodeposited Lithium Metal. *Nano Lett.* **17**, 1132–1139 (2017).
68. Sagane, F. *et al.* Effects of current densities on the lithium plating morphology at a lithium phosphorus oxynitride glass electrolyte/copper thin film interface. *J. Power Sources* **233**, 34–42 (2013).
69. Biswal, P., Stalin, S., Kludze, A., Choudhury, S. & Archer, L. A. Nucleation and Early Stage Growth of Li Electrodeposits. *Nano Lett.* **19**, 8191–8200 (2019).
70. Mohammadi, A., Monconduit, L., Stievano, L. & Younesi, R. Measuring the Nucleation Overpotential in Lithium Metal Batteries: Never Forget the Counter Electrode! *J. Electrochem. Soc.* **169**, 070509 (2022).
71. Seok, J., Gannett, C. N., Yu, S.-H. & Abruña, H. D. Understanding the Impacts of Li Stripping Overpotentials at the Counter Electrode by Three-Electrode Coin Cell Measurements. *Anal. Chem.* **93**, 15459–15467 (2021).
72. Oyakhire, S. T. *et al.* Electrical resistance of the current collector controls lithium morphology. *Nat. Commun.* **13**, 3986 (2022).
73. Guo, W. *et al.* Mixed Ion and Electron-Conducting Scaffolds for High-Rate Lithium Metal Anodes. *Adv. Energy Mater.* **9**, 1900193 (2019).
74. Park, S., Jin, H. & Yun, Y. S. Advances in the Design of 3D-Structured Electrode Materials for Lithium-Metal Anodes. *Adv. Mater.* **32**, 2002193 (2020).
75. Mohammadi, A. *et al.* Towards understanding the nucleation and growth mechanism of Li dendrites on zinc oxide-coated nickel electrodes. *J. Mater. Chem. A* **10**, 17593–17602 (2022).
76. Liu, Y. *et al.* Revealing and Elucidating ALD-Derived Control of Lithium Plating Microstructure. *Adv. Mater.* **10**, 1–11 (2020).
77. Zhou, Y. *et al.* Redistributing Li-Ion Flux by Parallely Aligned Holey Nanosheets for Dendrite-Free Li Metal Anodes. *Adv. Mater.* **32**, 2003920 (2020).
78. Lu, B. *et al.* Quantitatively Designing Porous Copper Current Collectors for Lithium Metal Anodes. *ACS Appl. Energy Mater.* **4**, 6454–6465 (2021).
79. Liu, Y. *et al.* Horizontal Stress Release for Protuberance-Free Li Metal Anode. *Adv. Funct. Mater.* **30**, 2002522 (2020).
80. Li, H. *et al.* Revealing Principles for Design of Lean-Electrolyte Lithium Metal Anode via In Situ Spectroscopy. *J. Am. Chem. Soc.* **142**, 2012–2022 (2020).
81. Gao, N. *et al.* Fast Diagnosis of Failure Mechanisms and Lifetime Prediction of Li Metal Batteries. *Small Methods* **5**, 1–11 (2021).
82. Younesi, R. & Bardé, F. Electrochemical performance and interfacial properties of Li-metal in lithium bis(fluorosulfonyl)imide based electrolytes. *Sci. Rep.* **7**, 3–8 (2017).
83. Yan, C. *et al.* Toward Critical Electrode/Electrolyte Interfaces in Rechargeable Batteries. *Adv. Funct. Mater.* **30**, 1909887 (2020).
84. Nilsson, V., Younesi, R., Brandell, D., Edström, K. & Johansson, P. Critical evaluation of the stability of highly concentrated LiTFSI - Acetonitrile electrolytes vs. graphite, lithium metal and LiFePO<sub>4</sub> electrodes. *J. Power Sources* **384**, 334–341 (2018).
85. Källquist, I. *et al.* Advances in studying interfacial reactions in rechargeable batteries by photoelectron spectroscopy. *J. Mater. Chem. A* (2022). doi:10.1039/D2TA03242B
86. Zheng, J. *et al.* Regulating electrodeposition morphology of lithium: Towards commercially relevant secondary Li metal batteries. *Chem. Soc. Rev.* **49**, 2701–2750 (2020).
87. Wu, H., Jia, H., Wang, C., Zhang, J. & Xu, W. Recent Progress in Understanding Solid Electrolyte Interphase on Lithium Metal Anodes. *Adv. Energy Mater.* **11**, 2003092 (2021).
88. Eshetu, G. G. *et al.* In-Depth Interfacial Chemistry and Reactivity Focused Investigation of Lithium-Imide- and Lithium-Imidazole-Based Electrolytes. *ACS Appl. Mater. Interfaces* **8**, 16087–16100 (2016).
89. An, S. J. *et al.* The state of understanding of the lithium-ion-battery graphite solid electrolyte interphase (SEI) and its relationship to formation cycling. *Carbon N. Y.* **105**, 52–76 (2016).
90. Aurbach, D. *et al.* On the Surface Chemical Aspects of Very High Energy Density, Rechargeable Li-Sulfur Batteries. *J. Electrochem. Soc.* **156**, A694 (2009).
91. Li, W. *et al.* The synergetic effect of lithium polysulfide and lithium nitrate to prevent lithium dendrite growth. *Nat. Commun.* **6**, 7436 (2015).
92. Jaumann, T. *et al.* Role of 1,3-Dioxolane and LiNO<sub>3</sub> Addition on the Long Term Stability of Nanostructured Silicon/Carbon Anodes for Rechargeable Lithium Batteries. *J. Electrochem. Soc.* **163**, A557–A564 (2016).
93. Etacheri, V. *et al.* Exceptional Electrochemical Performance of Si-Nanowires in 1,3-Dioxolane Solutions: A Surface Chemical Investigation. *Langmuir* **28**, 6175–6184 (2012).
94. Fiedler, C., Luerksen, B., Rohnke, M., Sann, J. & Janek, J. XPS and SIMS Analysis of Solid Electrolyte Interphases on Lithium Formed by Ether-Based Electrolytes. *J. Electrochem. Soc.* **164**, A3742–A3749 (2017).
95. Busche, M. R. *et al.* The Formation of the Solid/Liquid Electrolyte Interphase (SLEI) on NASICON-Type Glass

- Ceramics and LiPON. *Adv. Mater. Interfaces* **7**, 2000380 (2020).
96. Sharova, V. *et al.* Comparative study of imide-based Li salts as electrolyte additives for Li-ion batteries. *J. Power Sources* **375**, 43–52 (2018).
  97. Andersson, A. M., Herstedt, M., Bishop, A. G. & Edström, K. The influence of lithium salt on the interfacial reactions controlling the thermal stability of graphite anodes. *Electrochim. Acta* **47**, 1885–1898 (2002).
  98. Duangdangchote, S., Krittayavathananon, A., Phattharasupakun, N., Joraleechanchai, N. & Sawangphruk, M. Insight into the effect of additives widely used in lithium-sulfur batteries. *Chem. Commun.* **55**, 13951–13954 (2019).
  99. Louli, A. J. *et al.* Diagnosing and correcting anode-free cell failure via electrolyte and morphological analysis. *Nat. Energy* **5**, 693–702 (2020).
  100. Fang, C. *et al.* Pressure-tailored lithium deposition and dissolution in lithium metal batteries. *Nat. Energy* **6**, 987–994 (2021).

Table of Contents

